RSC Advances

PAPER

View Article Online
View Journal | View Issue

Cite this: *RSC Adv.*, 2025, **15**, 37183

Spectroscopic signatures of interfacial energy transfer in MoS_2-based van der Waals heterostructures under deep-UV excitation

Tsung-Hsien Lee,[a] Sheng-Lung Chou,[b] Tzu-Ping Huang,[b] Chak-Ming Liu,[b] Chih-Hao Chin,[b] Meng-Yeh Lin,[b] Hui-Fen Chen*[c] and Yu-Jong Wu *[ab]

Received 2nd July 2025
Accepted 15th September 2025

DOI: 10.1039/d5ra04686f

rsc.li/rsc-advances

We report a comprehensive photoluminescence (PL) and photoluminescence excitation (PLE) study of monolayer MoS_2 and its van der Waals heterostructures with hBN and graphene under deep-ultraviolet (DUV) excitation. Using synchrotron-based VUV/UV spectroscopy, we reveal that while pristine MoS_2 exhibits only A-exciton emission at ~660 nm under visible excitation, broadband near-infrared emission (750–900 nm) emerges at cryogenic temperatures under DUV excitation in MoS_2/hBN and MoS_2/graphene heterostructures. This emission indicates a nonlocal excitation–emission mechanism facilitated by interfacial energy transfer from the UV-absorbing layers. In MoS_2/hBN, a broad UV band near 350 nm also appears under 200 nm excitation and is attributed to impurity-related defect luminescence in hBN. The interfacial processes are governed by temperature-sensitive radiative channels involving defect-bound states or localized excitons in MoS_2. Our results highlight the crucial role of interlayer coupling and spectral sensitization in enabling new radiative pathways in 2D heterostructures, offering novel strategies for tailoring light emission in layered optoelectronic systems.

1. Introduction

Two-dimensional (2D) transition metal dichalcogenides (TMDCs), particularly monolayer molybdenum disulfide (MoS_2), have attracted intense interest for their unique optical and electronic properties.[1–10] Unlike graphene, which lacks a bandgap, monolayer MoS_2 exhibits a direct bandgap of ~1.8–1.9 eV, enabling strong photoluminescence (PL) in the visible to near-infrared region.[11–15] This makes MoS_2 a promising material for next-generation optoelectronic applications, including photodetectors, light-emitting diodes, and valleytronic devices. However, the low quantum yield of MoS_2 films which is limited by nonradiative recombination, intrinsic defects, and substrate-induced effects, remains a key challenge for practical implementation.[16–18]

To address these limitations, various strategies have been developed to enhance and modulate the PL response of MoS_2, including plasmonic coupling, defect passivation, dielectric environment tuning, and heterostructure engineering. Among these, constructing vertical van der Waals heterostructures with other 2D materials has proven particularly effective in modifying excitonic behavior, charge dynamics, and interfacial energy transfer.[19–29] For instance, graphene, with its high carrier mobility and gapless electronic structure, can efficiently quench MoS_2 emission *via* interlayer charge transfer.[30–35] In contrast, hexagonal boron nitride (hBN), a wide-bandgap (~6 eV), atomically flat insulator, offers a clean dielectric interface that preserves or enhances intrinsic PL of MoS_2 by suppressing nonradiative pathways.[36–40]

Beyond the visible regime, deep-ultraviolet (DUV) excitation offers access to higher-energy transitions in MoS_2 and its heterostructures, potentially enabling new radiative channels not observable under conventional visible excitation. However, the PL behavior of MoS_2-based heterostructures under vacuum ultraviolet (VUV) excitation remains largely unexplored, particularly with respect to interfacial energy transfer and defect-assisted emission at low temperatures. In this study, we investigate the photophysical response of monolayer MoS_2 and its heterostructures with hBN and graphene under synchrotron-based VUV/UV excitation. Using temperature-dependent PL and photoluminescence excitation (PLE) spectroscopy, we reveal the emergence of broadband near-infrared emission in MoS_2-based heterostructures upon deep-UV excitation. Our results show that this emission arises from an interlayer excitation–emission decoupling process, facilitated by energy transfer from hBN or graphene into MoS_2. These findings offer new insights into interfacial energy transfer mechanisms and highlight a novel route for controlling the optical response of

---

[a] *Department of Applied Chemistry and Institute for Molecular Science, National Yang Ming Chiao Tung University, Hsinchu 30010, Taiwan*

[b] *National Synchrotron Radiation Research Center, 101 Hsin-Ann Road, Hsinchu Science Park, Hsinchu 30076, Taiwan. E-mail: yjwu@nsrrc.org.tw*

[c] *Department of Medicinal and Applied Chemistry, Kaohsiung Medical University, 100, Shih-Chuan 1st Road, Kaohsiung 80708, Taiwan. E-mail: hfchen@kmu.edu.tw*

MoS_2 through far-UV sensitization and heterostructure engineering.

2. Experimental methods

Pristine MoS_2, hBN, and graphene thin films were purchased from ACS Material. These samples were fabricated by chemical vapor deposition (CVD) and subsequently transferred individually onto optical substrates (2 mm thick, Crystran) using a wet-transfer technique.[39] The dimensions of the thin films were 1 × 1 cm^2, mounted on 1-inch diameter optical substrates.

Photoabsorption and photoluminescence measurements were carried out at beamline BL03 of the Taiwan Light Source (TLS-BL03).[41–45] Synchrotron radiation was dispersed by a monochromator to provide photon energies ranging from 4 to 40 eV. The incident photon flux was monitored using a gold mesh (∼90% transmission) and recorded with a Keithley 6512 electrometer. A LiF or quartz window was employed as a cutoff filter to eliminate unwanted high-order high-energy photons from the beam.

Photoabsorption spectra were obtained by scanning photon energies over the 350–105 nm range with a 1 nm bandwidth. The VUV/UV light was transmitted perpendicularly through the thin film sample and subsequently detected *via* luminescence conversion using a sodium salicylate-coated window. The converted luminescence signal was collected by a photon-counting photomultiplier tube (PMT). The beam spot size was approximately 2 × 2 mm^2, allowing for reference signal (I_0) acquisition by shifting the beam to an uncoated region of the same optical window. Photoluminescence (PL) measurements were performed using the synchrotron radiation from TLS-BL03 as the excitation source. Emission signals were dispersed by a monochromator (Jobin-Yvon iHR320, 1 nm resolution) and detected by a photon-counting PMT (Hamamatsu R943-02). Photoluminescence excitation (PLE) spectra were recorded by monitoring the emission intensity at a fixed wavelength while scanning the excitation photon energy. Both PL and PLE spectra were corrected for the spectral response of the detection system and the excitation source. The temperature-dependent PL measurements were carried out using a closed-cycle helium cryostat system (ARS, DE-202) equipped with optical access and a temperature controller (Lakeshore 331), allowing precise regulation from 10 K to 300 K. The excitation power density during VUV-PL measurements was estimated to be $\sim 1 \times 10^{12}$ photons per s per cm^2 based on beamline calibration, and photobleaching behavior under prolonged exposure is attributed to UV-induced formation of sulfur vacancies in MoS_2.

Additional PL measurements under visible-light excitation were performed using a commercial spectrometer (FS5, Edinburgh Instruments). Raman spectra were collected using a home-built confocal micro-Raman spectroscopy system equipped with a 532 nm DPSS laser (50 mW), a monochromator (iHR320, HORIBA) with a 1200 lines per mm diffraction grating, and a thermoelectrically cooled CCD detector (Newton DU970P-BVF, ANDOR). The system provided a spectral resolution of 1.5 cm^{-1} around 550 nm. The atomic force microscope (AFM) images were acquired with an AFM (NTEGRA II, NT-MDT) in contact mode under ambient condition. A silicon cantilever (NSG30, YFQ Technology Co., Ltd) with an Au-coated reflective side and a nominal spring constant of 22 N m^{-1} was used. The line scan rate was 0.4 Hz. Images were acquired over a 20 × 20 μm^2 area. The spatial resolution along the *X* and *Y*-axes was 4.6 nm and 0.67 nm along the *Z*-axis.

3. Results and discussion

3.1. Raman and AFM characterization

Raman spectroscopy was employed to investigate the structural and vibrational properties of the MoS_2 thin films and their heterostructures. Fig. 1 shows the Raman spectra of MoS_2 films deposited on MgF_2, hBN, and graphene substrates. Two prominent first-order Raman-active modes of MoS_2, corresponding to the in-plane E^1_{2g} and out-of-plane A_{1g} phonon modes,[46] were observed in all samples. For MoS_2 films on MgF_2 substrates, the E^1_{2g} and A_{1g} modes were located at 383.6 and 409.0 cm^{-1}, respectively, yielding a frequency separation (Δ) of 25.4 cm^{-1}. Compared to previously reported values for monolayer MoS_2,[47] where Δ typically falls within 19–20 cm^{-1}, this larger separation indicates the presence of few-layer MoS_2, approximately 4–5 layers. The increased Δ value may be attributed to strain effects and interlayer interactions induced by the lattice mismatch between the hexagonal MoS_2 and the cubic MgF_2 substrate, as well as possible roughness or residual stress introduced during the wet-transfer process.

In the MoS_2/hBN heterostructure, both the E^1_{2g} and A_{1g} modes exhibited slight shifts to 385.9 and 405.9 cm^{-1}, respectively, resulting in a frequency separation of 20.0 cm^{-1}. This value closely matches that of monolayer MoS_2, suggesting that the MoS_2 film maintains its monolayer nature when supported on hBN. The relatively small lattice mismatch and excellent lattice compatibility between MoS_2 and hBN, both possessing hexagonal crystal symmetry, effectively minimize interfacial strain during the transfer process.[38,40] Additionally, Raman

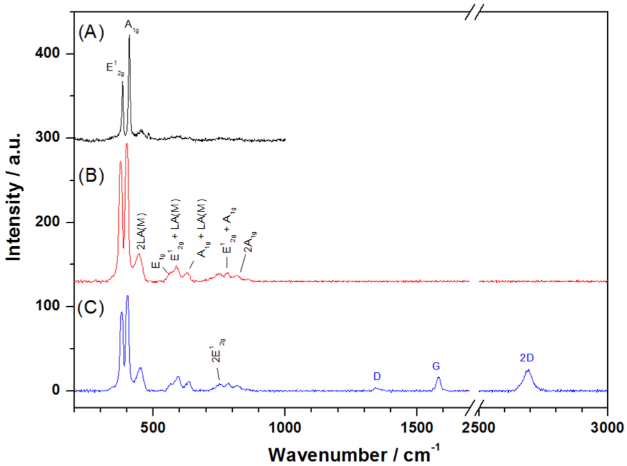

Fig. 1 Raman spectra of (A) MoS_2 thin film, (B) MoS_2/hBN heterostructure, and (C) MoS_2/graphene heterostructure on MgF_2 substrates. Characteristic vibrational modes of MoS_2 and graphene are labeled in black and blue, respectively.

signals from the hBN layer were not observed, likely due to the intrinsically weak Raman activity of single-layer hBN.[44] However, complementary UV absorption measurements confirmed the presence of hBN in the heterostructure, as discussed in Section 3.2. In contrast, the MoS_2/graphene heterostructure exhibited additional Raman features characteristic of graphene, including the G band (~1589 cm^{-1}) and the 2D band (~2700 cm^{-1}). The observation of the weak D band (~1350 cm^{-1}) indicates that the graphene layer exhibits less defects. The E^1_{2g} and A_{1g} modes of MoS_2 in this heterostructure were observed at 384.9 and 405.8 cm^{-1}, respectively, resulting in a frequency separation of 20.9 cm^{-1}. This separation is consistent with monolayer MoS_2, suggesting that both the MoS_2 and graphene layers in the heterostructure are single layers.

In addition to the characteristic first-order E^1_{2g} and A_{1g} modes of MoS_2 near 380 and 405 cm^{-1}, prominent Raman features are observed in the 500–800 cm^{-1} region for the MoS_2/hBN and MoS_2/graphene heterostructures. These additional peaks correspond to second-order and combination modes such as 2LA(M), E^1_{2g} + LA(M), and A_{1g} + LA(M), which are notably enhanced under 532 nm excitation. Although monolayer MoS_2 typically exhibits weak second-order Raman bands, their relative intensity becomes significantly stronger in the heterostructures. This enhancement may arise from resonance Raman scattering, where the 532 nm excitation lies near the A-exciton absorption of MoS_2 (~1.88 eV), thereby increasing the scattering cross-section for multi-phonon processes. Moreover, the presence of atomically thin hBN or graphene beneath the MoS_2 layer can modify the local dielectric environment and introduce interfacial strain or phonon coupling, which may further promote phonon-assisted scattering pathways. The observation of these pronounced high-order modes suggests strong exciton–phonon interactions and underscores the influence of interfacial effects in modifying the vibrational response of 2D heterostructures. On the other hand, the reduced frequency separation (Δ) = 20.9 cm^{-1} in MoS_2/graphene, compared to monolayer MoS_2, arises from the interplay of charge transfer and strain effects. The interfacial electron transfer that selectively softens A_{1g}, and modest tensile strain that shifts E^1_{2g} more strongly than A_{1g}. In MoS_2/hBN, where charge transfer is strongly suppressed, (Δ) ≈ 20.0 cm^{-1} instead reflects near-intrinsic monolayer behavior. These results align with previous reports on doping- and strain-induced Raman shifts in MoS_2.[32,48,49]

AFM measurements were performed on the transferred MoS_2 thin films deposited on MgF_2, as well as on MoS_2/hBN and MoS_2/graphene heterostructures, as shown in Fig. 2. The topography scans (20 μm × 20 μm) reveal continuous coverage across the scanned areas, with only minor corrugations and transfer-related wrinkles that are commonly observed in mechanically laminated 2D films. The root-mean-square (RMS) surface roughness values are 1.41 nm for MoS_2/MgF_2, 1.40 nm for MoS_2/hBN/MgF_2, and 1.58 nm for MoS_2/graphene/MgF_2, respectively. These values confirm that the films are smooth and laterally uniform, with no evidence of cracks or large voids across the probed regions. Given that the optical excitation beam diameter (~2 mm) is much larger than the AFM scan window, the absence of large-area defects ensures that the probed regions in our spectroscopic measurements are representative of well-formed van der Waals heterointerfaces. Because the commercial films were supplied on PMMA-coated carrier substrates, it was not possible to perform Raman characterization of the as-grown MoS_2 prior to transfer, nor to capture a clear step-height profile for thickness verification in our AFM scans. Nevertheless, the observed morphology is fully consistent with monolayer MoS_2 coverage and supports the conclusion that the anomalous Raman mode separation observed on MgF_2 arises from substrate-induced strain and interfacial coupling, rather than from multilayer contamination.

Overall, the Raman and AFM analysis confirm the successful fabrication of high-quality MoS_2/hBN and MoS_2/graphene heterostructures while preserving the crystallinity of the MoS_2 films. The observed variations in peak positions and frequency separations reflect the subtle influence of different substrates and heterointerfaces on the vibrational and electronic properties of the MoS_2 layers.

3.2. Absorptions and PL of pristine MoS_2 thin films

The absorption spectra of the MoS_2 thin films were systematically measured over a broad photon energy range from the visible to the far-ultraviolet region. As shown in Fig. 3, in the visible spectral region, two pronounced excitonic absorption features were observed at approximately 665 nm (~1.86 eV) and 616 nm (~2.01 eV), which are attributed to the A- and B-exciton transitions, respectively.[11,12] These arise from transitions between the spin–orbit-split valence band maxima (K_{v1} and K_{v2}) and the conduction band minimum (K_c), in excellent agreement with both theoretical predictions[50,51] and previous optical absorption measurements.[11,12] The spin–orbit coupling of the valence band leads to the splitting between the A- and B-exciton states, which is typically ~150–200 meV. As the excitation photon energy increases (λ < 450 nm), a broad absorption shoulder appears between 400–450 nm (~2.75–3.1 eV). This feature is associated with the so-called C-exciton, which stems from transitions near the Γ or Q points in the Brillouin zone where the conduction bands become flatter and more densely packed, leading to enhanced joint density of states.[50,51]

In the deep-UV region (125–300 nm), the absorption increases steadily without distinct peaks,[52,53] consistent with transitions to higher-lying conduction band states.[50] These states lie well above the quasiparticle gap and involve more delocalized interband transitions, possibly extending to the continuum. The QSGW calculations show that these higher-energy states are separated from the K-point conduction band minimum by several electron volts and thus are only accessible with deep-UV excitation sources.[50] Importantly, the presence of substantial absorption at wavelengths below 300 nm (~4.1 eV and above) provides an energetic window for exciting hot carriers or higher-lying excitonic states, which are often not probed in conventional visible-light photoluminescence studies. These VUV transitions set the stage for the observation

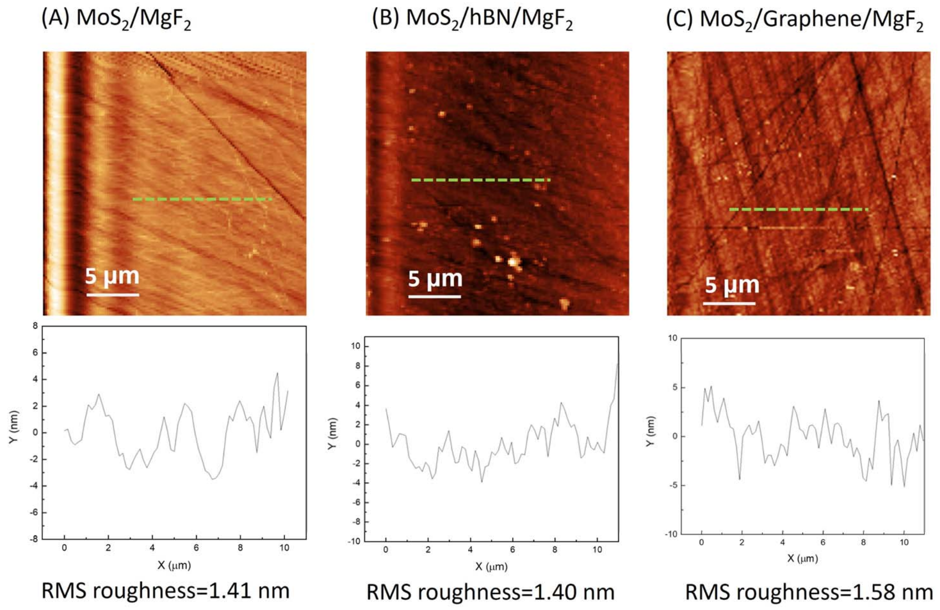

Fig. 2 AFM topography (20 µm × 20 µm) of transferred MoS$_2$ thin films on (A) MgF$_2$, (B) hBN/MgF$_2$, and (C) graphene/MgF$_2$ substrates.

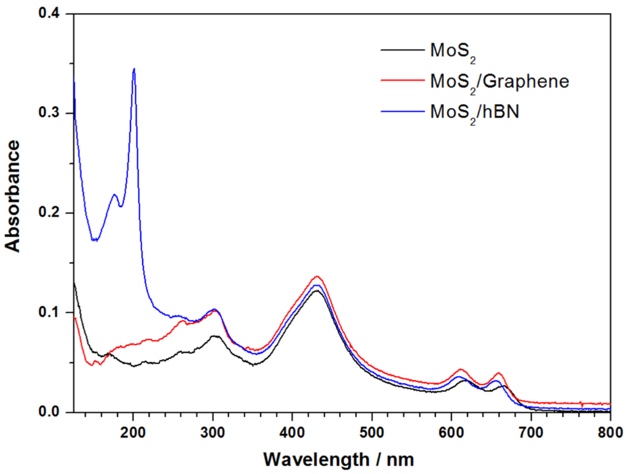

Fig. 3 Absorption spectra of MoS$_2$, MoS$_2$/graphene, and MoS$_2$/hBN thin films on MgF$_2$ substrates at 295 K.

of broadband emission under deep-UV excitation, as will be discussed later.

Photoluminescence measurements under different excitation conditions revealed a strong dependence on both temperature and photon energy, as shown in Fig. 4. Under room-temperature excitation with visible light (*e.g.*, 430 nm), a sharp emission band centered around 670 nm was detected, corresponding to the radiative recombination of the A-exciton. The PLE spectrum monitored at 670 nm shows a broad response from 400 to 500 nm, consistent with A- and B-exciton resonances and the C-exciton absorption shoulder.[11,12,14,15] No additional emission was observed when excitation wavelengths below 300 nm were used at room temperature, indicating that high-energy excitation alone is insufficient to produce radiative recombination under thermalized conditions. However, under cryogenic conditions (10 K), excitation with UV light at 260 nm and 300 nm induced a distinct, broad emission band arising near 690 nm, extending toward 900 nm. This broadband luminescence is fundamentally different from the A-exciton emission observed under visible excitation. It cannot be reproduced by any excitation wavelength in the visible or UV range at room temperature. To further elucidate the nature of the broadband emission observed under VUV excitation, temperature-dependent PL measurements were conducted from 10 K to 300 K under 300 nm excitation, as shown in Fig. 5.

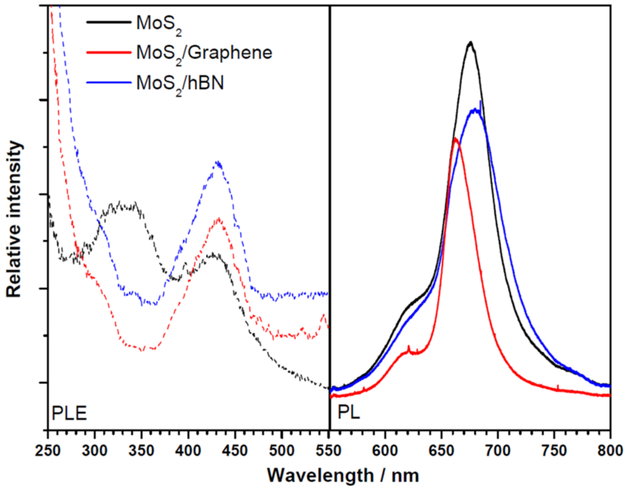

Fig. 4 PL spectra (solid curve) of MoS$_2$, MoS$_2$/graphene, and MoS$_2$/hBN thin films on MgF$_2$ substrates at 295 K under 430 nm excitation. The corresponding PLE spectra (dash curve) were obtained by monitoring the intensity variation of the characteristic PL band of each sample.

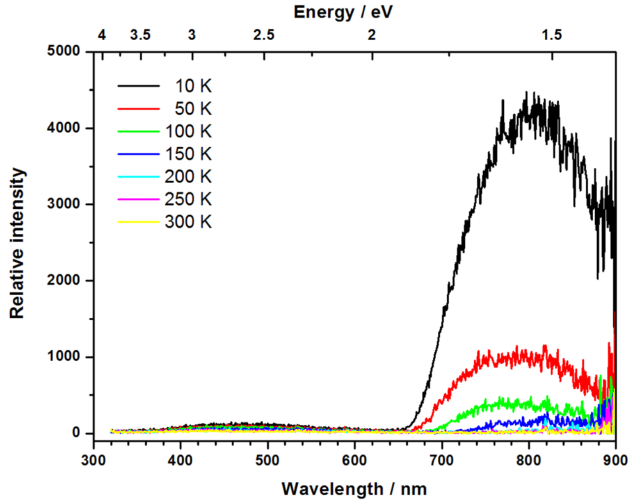

Fig. 5 PL spectra of MoS_2 thin films on MgF_2 substrates at various temperatures under 300 nm excitation.

At 10 K, the emission was most intense, but as the temperature increased, the PL intensity rapidly decreased and was nearly quenched above 250 K. This thermal quenching behavior suggests that the broadband luminescence originates from defect-bound states or localized excitons that become thermally delocalized at elevated temperatures. The activation of non-radiative recombination pathways and thermal escape of carriers from shallow defect traps at higher temperatures effectively suppress the radiative recombination channels responsible for this emission.[54]

The emergence of broadband emission under UV excitation and low temperature is attributed to defect-assisted recombination and high-energy carrier relaxation processes. Excitation at energies above ~4.1 eV may promote electrons to higher conduction bands, followed by phonon scattering or trapping at sub-gap defect states, which enables radiative recombination pathways not otherwise accessible. At low temperatures, non-radiative decay channels are suppressed, and thermal detrapping is reduced, allowing these defect-related luminescence channels to dominate. The absence of this emission at room temperature is likely due to thermal escape of carriers from shallow traps and activation of nonradiative recombination channels, as commonly reported in temperature-dependent studies of MoS_2.[54–56] The thermal quenching of broadband emission is attributed to thermally activated delocalization of carriers from shallow defect states, enhanced phonon-assisted nonradiative decay, and increased carrier–phonon scattering at elevated temperatures. These processes reduce the population of radiatively active localized states and suppress defect-assisted emission, consistent with previous studies on low-temperature PL behavior in MoS_2. In contrast, pure MgF_2 substrates under identical excitation conditions do not exhibit such broadband emission, confirming that the observed luminescence originates from the MoS_2 layer itself rather than the substrate or its intrinsic defects. The broadband emission is attributed to radiative recombination *via* defect-bound states or localized excitons stabilized at cryogenic temperatures. While the spectral shape and thermal behavior strongly suggest defect-assisted processes, further investigation (*e.g.*, time-resolved PL or low-temperature near-field imaging) is needed to definitively distinguish between static defect trapping and confinement-induced localization.

Additionally, we observed that prolonged exposure of the MoS_2 thin films to ultraviolet excitation leads to a gradual decrease in PL intensity over time. The observed photobleaching behavior under continuous UV excitation may be associated with the photoinduced desorption of sulfur atoms from the MoS_2 lattice. The photon energies used in this study, particularly below 300 nm, are sufficient to break Mo–S bonds, potentially leading to the formation of sulfur vacancies. These defect sites can initially enhance defect-related emission,[24,29] but may subsequently serve as nonradiative recombination centers as their density increases, thereby reducing the overall PL intensity.

3.3. Absorptions and PL in MoS_2/hBN and MoS_2/graphene heterostructures

Fig. 3 compares the absorption spectra of MoS_2, MoS_2/hBN, and MoS_2/graphene heterostructures on MgF_2 substrates. In the visible region, all three samples exhibit prominent absorption peaks near 1.85 and 2.0 eV (~670 and ~620 nm), corresponding to the A and B excitonic transitions of monolayer MoS_2.[11,12] However, slight variations in positions, intensity and spectral shape are observed for the heterostructures. These changes may arise from interfacial interactions or substrate-induced strain,[13] but are relatively minor compared to changes observed in the deep-UV region.

In the deep-UV region (~200 nm and below), the MoS_2/hBN and MoS_2/graphene samples show significant increases in absorbance compared to pristine MoS_2. This enhancement is not solely attributed to MoS_2 but rather originates from the intrinsic optical transitions of the constituent hBN and graphene layers. In our previous work, monolayer hBN exhibits a strong absorption band at ~6.1 eV (~203 nm),[44] corresponding to the $\pi \rightarrow \pi^*$ transition near the K point of the Brillouin zone, which is associated with direct excitons in monolayer hBN. Similarly, the enhanced deep-UV absorbance in the MoS_2/graphene heterostructure can be partly attributed to the $\pi \rightarrow \pi^*$ transitions of graphene, which exhibit broad absorption features extending into the deep-UV regime due to its semi-metallic band structure with a vanishing density of states at the Dirac point.[42,43] It is important to note that the observed increase in absorbance below 220 nm may also be partially influenced by increased light scattering due to surface roughness or non-uniform stacking in the heterostructures. This possibility arises from the imperfect planar interfaces formed during the layer-transfer process.

To explore the influence of supporting 2D materials on the optical response of MoS_2, we examined the PL and PLE spectra of MoS_2/hBN and MoS_2/graphene heterostructures at 300 and 10 K. As comparison of PL spectra upon excitation with 430 nm in Fig. 4, pristine monolayer MoS_2 exhibits the highest PL intensity centered around 660 nm. When interfaced with graphene, the PL intensity is markedly quenched, suggesting efficient nonradiative energy or charge transfer from MoS_2 to graphene due to high carrier mobility and zero bandgap of graphene.[31,32,35] In contrast, the MoS_2/hBN heterostructures maintains a PL intensity comparable to or slightly higher than pristine MoS_2, indicating minimal interfacial quenching. Upon deep-UV excitation, as shown in Fig. 6, both heterostructures exhibit broadband near-infrared PL centered above 750 nm when excited at short wavelengths, in contrast to pristine MoS_2, which shows no detectable emission under the same excitation conditions. This broadband luminescence is most prominent in the MoS_2/hBN sample when excited at 200 nm, and also appears in MoS_2/graphene under 260 nm excitation. Notably, no emission is observed from the underlying MgF_2 substrate under any conditions. Fig. 5 depicts the corresponding PLE spectra, monitored at 750–785 nm emission wavelengths, further confirming that the excitation profiles of the heterostructures differ markedly from that of MoS_2 alone. In the MoS_2/hBN sample, a sharp PLE peak near 200 nm is observed, consistent with the known deep-UV absorption band of monolayer hBN.[44] Similarly, the MoS_2/graphene sample shows enhanced excitation response around 260 nm, aligning with the strong absorption of graphene in the far-UV regime.[43] These results clearly indicate that the deep-UV excitation leading to broadband emission in MoS_2 is enabled only when a second absorbing 2D layer (hBN or graphene) is present. Under the same excitation, pristine MoS_2 does not exhibit this emission, implying that the heterostructure architecture plays a critical role in facilitating this process.

In addition to low-temperature results, PL spectra were also acquired at room temperature to evaluate the thermal stability of the broadband emission in MoS_2-based heterostructures. As shown in Fig. 7, the broad emission band centered around 350 nm observed upon 200 nm excitation is attributed to defect-related luminescence from the hBN layer. This emission likely arises from impurity-induced states, such as those associated with oxygen or carbon atoms incorporated during the CVD growth process.[57] These defects form donor–acceptor pairs that facilitate radiative recombination at energies significantly lower than the intrinsic excitonic emission of hBN. The absence of this band under longer-wavelength excitation further supports

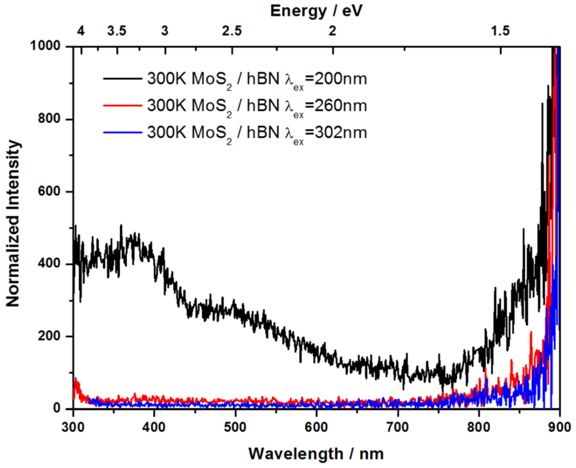

Fig. 7 PL spectra of MoS_2/hBN thin films on MgF_2 substrates at 300 K under excitation with various wavelengths.

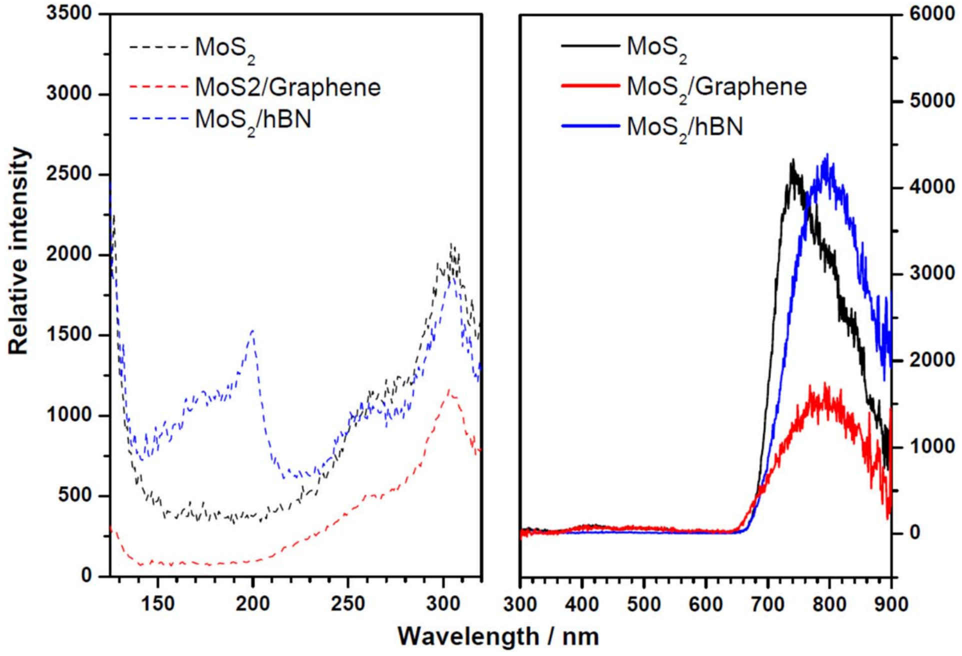

Fig. 6 PL spectra (solid curve) of MoS_2, MoS_2/graphene, and MoS_2/hBN thin films on MgF_2 substrates at 10 K under 260 nm excitation. The corresponding PLE spectra (dash curve) were obtained by monitoring the intensity variation of the characteristic PL band of each sample.

its origin from deep-level states that require high-energy photons for activation. The emission intensity gradually decreases with longer excitation wavelengths and becomes negligible beyond 300 nm. This indicates that excitation near the π–π* transition of hBN (∼6.2 eV) remains an effective pathway to generate broadband luminescence from the MoS_2 layer even at ambient conditions, albeit at a reduced efficiency compared to 10 K.

Similarly, in the MoS_2/graphene sample (Fig. 8), detectable broadband emission is observed at room temperature under deep-UV excitation. Excitation at 220–130 nm yields a relatively flat emission profile, with intensity centered in the 400–800 nm range. The signal strength diminishes with increasing excitation wavelength and becomes negligible at 300 nm. This suggests that high-energy excitation of graphene's π-electron system can still trigger emissive states in the MoS_2 layer, although with significant thermal quenching compared to cryogenic measurements. Although MoS_2-based heterostructures exhibit broadband emission features under deep-UV excitation, the PLQY measured at 430 nm excitation shows no significant enhancement compared to pristine MoS_2. This is likely due to the absorption being dominated by the top MoS_2 layer, limiting interlayer excitation dynamics, and the instrumental cutoff of the commercial spectrometer beyond 850 nm, which restricts detection of the far-IR emission components.

Additionally, from the Raman spectra (Fig. 1), we evaluated the wavenumber positions of the E^1_{2g} and A_{1g} modes across the sample and constructed a correlative plot to extract strain and doping values. Using the linear decoupling method described in previous studies,[58–60] we find that the MoS_2 in the heterostructures exhibits a tensile strain of approximately 0.20–0.25% and an n-type doping level of $(0.9–1.1) \times 10^{12}$ cm^{-2}. In contrast, we also used the shift of the A exciton peak (Fig. 4) to estimate the biaxial strain. However, strain estimates derived from A exciton PL peak shifts (∼0.05–0.07%) are lower than those obtained from Raman analysis (∼0.20–0.25%), likely due to differences in how these two techniques respond to local doping, substrate dielectric screening, and exciton binding energy. Such variation is consistent with previous reports where PL and Raman diagnostics yield complementary but non-identical strain values in monolayer TMDCs.

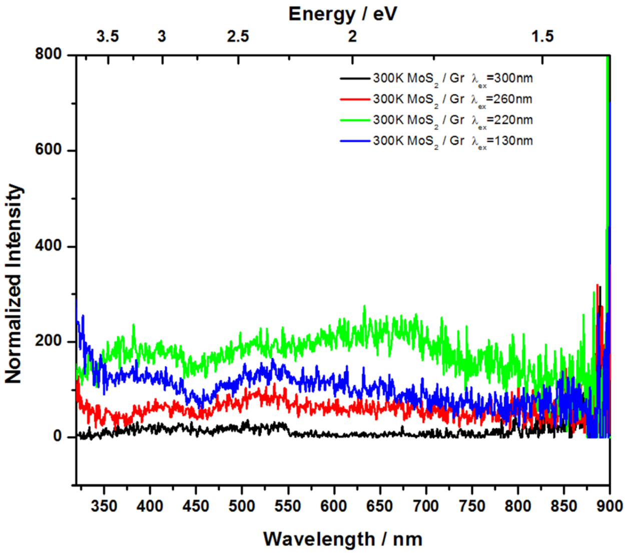

Fig. 8 PL spectra of MoS_2/graphene thin films on MgF_2 substrates at 300 K under excitation with various wavelengths.

Overall, while both MoS_2/hBN and MoS_2/graphene heterostructures retain their ability to produce broadband PL under vacuum ultraviolet excitation at room temperature, the emission intensity is notably reduced due to increased nonradiative losses. These results reinforce the role of high-energy absorbing layers (hBN or graphene) in sensitizing the MoS_2 emission response beyond its intrinsic excitation range, and highlight the temperature dependence of this nonlocal excitation–emission process.

3.4. Radiative mechanism and interfacial energy transfer pathways

The PL behavior of MoS_2 undergoes striking modification when incorporated into van der Waals heterostructures with hBN or graphene. As demonstrated in the previous sections, broadband near-infrared emission in the 750–900 nm range is observed at 10 K in both MoS_2/hBN and MoS_2/graphene systems under deep-UV excitation ($\lambda < 260$ nm), whereas pristine MoS_2 exhibits no such emission under the same conditions. This indicates that the initial photoexcitation occurs primarily in the hBN or graphene layers, followed by an interfacial energy transfer into the MoS_2 layer, where radiative recombination takes place.

In the MoS_2/hBN heterostructure, the broadband emission is efficiently triggered by ∼200 nm excitation, resonant with the π–π* transitions of hBN centered at ∼6.1 eV. Similarly, in the MoS_2/graphene system, the emission is most pronounced under ∼260 nm excitation, aligning with the broad π-electron absorption continuum of graphene. These observations imply an excitation–emission decoupling mechanism, where the absorption of high-energy photons occurs in one material (donor), and the emission is generated in another (acceptor).

Two primary mechanisms may account for this interfacial coupling: nonradiative energy transfer and carrier tunneling.[61–65] Nonradiative Förster resonance energy transfer (FRET) can occur between the UV-absorbing layer (hBN or graphene) and MoS_2 if the donor emission overlaps with the acceptor absorption and the separation is within the Förster radius (∼1–10 nm). Alternatively, photoexcited hot carriers or excitons in hBN or graphene may tunnel across the interface into localized or defect-related states in MoS_2, followed by radiative recombination. At cryogenic temperatures, these defect-bound excitons become stabilized due to suppressed thermal delocalization, resulting in strong broadband luminescence. This emission rapidly quenches at higher temperatures (above ∼250 K), consistent with thermally activated nonradiative decay and carrier escape from shallow trap states. The higher emission intensity in MoS_2/hBN compared to MoS_2/graphene is likely due to the atomically smooth, insulating nature of hBN, which minimizes interfacial electronic dissipation and promotes longer exciton lifetimes.

The contrasting effects of hBN and graphene on the photoluminescence behavior of MoS_2 originate from their fundamentally different electronic structures. hBN is a wide-bandgap (~6.1 eV) insulator with no available electronic states near the Fermi level or the MoS_2 conduction/valence bands. As such, it suppresses interlayer charge transfer, preserving the radiative recombination in MoS_2. This insulating character allows energy absorbed in hBN (*e.g.*, through π–π transitions) to be non-radiatively transferred into MoS_2, populating localized or defect-bound states that emit in the near-infrared under cryogenic conditions.

In contrast, graphene exhibiting the gapless electronic structure and high density of available states around the Fermi level enable ultrafast interlayer charge transfer. Under visible excitation, this leads to quenching of the MoS_2 exciton emission. However, under deep-UV excitation, graphene absorbs high-energy photons and can generate hot carriers, some of which may tunnel across the interface into MoS_2. These carriers may become trapped at defect sites, giving rise to broadband luminescence. Compared to hBN, the PL intensity in MoS_2/graphene is weaker due to competing nonradiative dissipation in the conductive graphene layer.

The findings demonstrate that heterostructure assembly can be used to activate otherwise inaccessible optical channels in MoS_2. By tailoring the spectral absorption properties of adjacent 2D layers and optimizing the interfacial contact, excitation–emission decoupling can be employed to extend the functional spectral range of TMDCs. This principle offers a new paradigm for engineering light–matter interactions in low-dimensional systems, enabling the design of devices where absorption and emission are spatially and energetically separated.

4. Conclusion and outlook

This work explores the photophysical behavior of monolayer MoS_2 on MgF_2 and in heterostructures with hBN and graphene. While visible excitation yields the well-known A-exciton emission at 660 nm, deep-UV excitation (<300 nm) only activates a broad near-infrared emission (750–900 nm) at cryogenic temperatures, revealing the role of defect or trap-assisted radiative channels. In MoS_2/hBN and MoS_2/graphene systems, far-UV absorption in the supporting layers can sensitize MoS_2 emission *via* interfacial energy transfer. This excitation–emission decoupling suggests mechanisms such as nonradiative dipole coupling or hot carrier tunneling across clean van der Waals interfaces. Our results demonstrate a novel route to access hidden radiative states in MoS_2 through heterostructure design and UV sensitization.

Future work could focus on time-resolved spectroscopy to further unravel the ultrafast dynamics of the energy transfer processes, as well as theoretical modeling of interlayer exciton formation in MoS_2-based heterostructures. Moreover, the role of interfacial strain, dielectric screening, and stacking order in modulating the radiative behavior warrants further exploration. Ultimately, these results open new avenues for designing hybrid 2D systems with tunable optical functionalities driven by van der Waals interface physics.

Author contributions

T. H. L. and S. L. C. contributed equally to this work. T. H. L., S. L. C., C. H. C., and M. Y. L. conducted the absorption and photoluminescence measurements. T. P. H. carried out the Raman measurements. C. M. L. performed AFM measurements. H. F. C. performed data analysis and prepared the initial draft of the manuscript. Y. J. W. finalized and wrote the manuscript. All authors reviewed and approved the final version of the manuscript.

Conflicts of interest

There are no conflicts to declare.

Data availability

The data supporting the findings of this study are available in the article. The raw data supporting the findings of this study are available from the corresponding author upon reasonable request.

Acknowledgements

This work was supported by the National Science and Technology Council of Taiwan (grants NSTC 114-2639-M-A49-002-ASP and NSTC 114-2113-M-213-002) and the National Synchrotron Radiation Research Center. We thank Dr Chia-Hao Chen at NSRRC for discussion of AFM data.

References

1 H. Wang, H. Yuan, S. S. Hong, Y. Li and Y. Cui, Physical and Chemical Tuning of Two-Dimensional Transition Metal Dichalcogenides, *Chem. Soc. Rev.*, 2015, **44**, 2664–2680.
2 S. Najmaei, X. Zou, D. Er, J. Li, Z. Jin, W. Gao, Q. Zhang, S. Park, L. Ge, S. Lei, J. Kono, V. B. Shenoy, B. I. Yakobson, A. George, P. M. Ajayan and J. Lou, Tailoring the Physical Properties of Molybdenum Disulfide Monolayers by Control of Interfacial Chemistry, *Nano Lett.*, 2014, **14**, 1354–1361.
3 M. Chhowalla, H. S. Shin, G. Eda, L.-J. Li, K. P. Loh and H. Zhang, The Chemistry of Two-Dimensional Layered Transition Metal Dichalcogenide Nanosheets, *Nat. Chem.*, 2013, **5**, 263–275.
4 C. R. Ryder, J. D. Wood, S. A. Wells and M. C. Hersam, Chemically Tailoring Semiconducting Two-Dimensional Transition Metal Dichalcogenides and Black Phosphorus, *ACS Nano*, 2016, **10**, 3900–3917.
5 R. Lv, J. A. Robinson, R. E. Schaak, D. Sun, Y. Sun, T. E. Mallouk and M. Terrones, Transition Metal Dichalcogenides and Beyond: Synthesis, Properties, and Applications of Single- and Few-Layer Nanosheets, *Acc. Chem. Res.*, 2014, **48**, 56–64.
6 M. Chhowalla, Z. Liu and H. Zhang, Two-Dimensional Transition Metal Dichalcogenide (TMD) Nanosheets, *Chem. Soc. Rev.*, 2015, **44**, 2584–2586.

7 Y. Shi, H. Li and L.-J. Li, Recent Advances in Controlled Synthesis of Two-Dimensional Transition Metal Dichalcogenides *Via* Vapour Deposition Techniques, *Chem. Soc. Rev.*, 2015, **44**, 2744–2756.

8 W. Choi, N. Choudhary, G. H. Han, J. Park, D. Akinwande and Y. H. Lee, Recent development of two-dimensional transition metal dichalcogenides and their applications, *Mater. Today*, 2017, **20**, 116–130.

9 O. Salehzadeh, N. H. Tran, X. Liu, I. Shih and Z. Mi, Exciton kinetics, quantum efficiency, and efficiency drop of monolayer MoS_2 light-emitting devices, *Nano Lett.*, 2014, **14**, 4125–4130.

10 Q. H. Wang, K. Kalantar-Zadeh, A. Kis, J. N. Coleman and M. S. Strano, Electronics and optoelectronics of two-dimensional transition metal dichalcogenides, *Nat. Nanotechnol.*, 2012, **7**, 699–712.

11 A. Splendiani, L. Sun, Y. Zhang, T. Li, J. Kim, C.-Y. Chim, G. Galli and F. Wang, Emerging Photoluminescence in Monolayer MoS_2, *Nano Lett.*, 2010, **10**, 1271–1275.

12 G. Eda, H. Yamaguchi, D. Voiry, T. Fujita, M. Chen and M. Chhowalla, Photoluminescence from Chemically Exfoliated MoS_2, *Nano Lett.*, 2011, **11**, 5111–5116.

13 H. J. Conley, B. Wang, J. I. Ziegler, R. F. Haglund Jr, S. T. Pantelides and K. I. Bolotin, Bandgap Engineering of Strained Monolayer and Bilayer MoS_2, *Nano Lett.*, 2013, **13**, 3626–3630.

14 A. Steinhoff, J.-H. Kim, F. Jahnke, M. Rösner, D.-S. Kim, C. Lee, G. H. Han, M. S. Jeong, T. O. Wehling and C. Gies, Efficient Excitonic Photoluminescence in Direct and Indirect Band Gap Monolayer MoS_2, *Nano Lett.*, 2015, **15**, 6841–6847.

15 B. G. Shin, G. H. Han, S. J. Yun, H. M. Oh, J. J. Bae, Y. J. Song, C.-Y. Park and Y. H. Lee, Indirect Bandgap Puddles in Monolayer MoS_2 by Substrate-Induced Local Strain, *Adv. Mater.*, 2016, **28**, 9378–9384.

16 S. Hwangbo, L. Hu, A. T. Hoang, J. Y. Choi and J. H. Ahn, Wafer-scale monolithic integration of full-colour micro-LED display using MoS_2 transistor, *Nat. Nanotechnol.*, 2022, **17**, 500–506.

17 G. Swain, G. J. Choi, J. S. Gwag and Y. Kim, Monolayer MoS_2 and WS_2 for Vertical Circular-Polarized-Light-Emitting Diode: from Fundamental Understanding to Device Architecture, *Adv. Electron. Mater.*, 2025, **11**, 2400381.

18 M. Long, P. Wang, H. Fang and W. Hu, Progress, Challenges, and Opportunities for 2D Material Based Photodetectors, *Adv. Funct. Mater.*, 2019, **29**, 1803807.

19 Z.-Q. Wu, J.-L. Yang, N. K. Manjunath, Y.-J. Zhang, S.-R. Feng, Y.-H. Lu, J.-H. Wu, W.-W. Zhao, C.-Y. Qiu, J.-F. Li and S.-S. Lin, Gap-Mode Surface-Plasmon-Enhanced Photoluminescence and Photoresponse of MoS_2, *Adv. Mater.*, 2018, **30**, 1706527.

20 A. Bera, D. V. S. Muthu and A. K. Sood, Enhanced Raman and photoluminescence response in monolayer MoS_2 due to laser healing of defects, *J. Raman Spectrosc.*, 2018, **49**, 100–105.

21 S. V. Sivaram, A. T. Hanbicki, M. R. Rosenberger, G. G. Jernigan, H. J. Chuang, K. M. McCreary and B. T. Jonker, Spatially selective enhancement of photoluminescence in MoS_2 by exciton-mediated adsorption and defect passivation, *ACS Appl. Mater. Interfaces*, 2019, **11**, 16147–16155.

22 H. Nan, Z. Wang, W. Wang, Z. Liang, Y. Lu, Q. Chen, D. He, P. Tan, F. Miao, X. Wang, J. Wang and Z. Ni, Strong Photoluminescence Enhancement of MoS_2 through Defect Engineering and Oxygen Bonding, *ACS Nano*, 2014, **8**, 5738–5745.

23 Z. Li, Z. Chen, L. Xiao, X. Zhou, C. Zhao and Y. Zhang, Extremely Enhanced Photoluminescence in MoS_2-Derived Quantum Sheets, *ACS Appl. Mater. Interfaces*, 2024, **16**, 15487–15495.

24 Y. Zeng, W. Chen, B. Tang, J. Liao, J. Lou and Q. Chen, Synergetic photoluminescence enhancement of monolayer MoS_2 *via* surface plasmon resonance and defect repair, *RSC Adv.*, 2018, **8**, 23591–23598.

25 L. P. Mawlong, K. K. Paul and P. K. Giri, Direct chemical vapor deposition growth of monolayer MoS_2 on TiO_2 nanorods and evidence for doping-induced strong photoluminescence enhancement, *J. Phys. Chem. C*, 2018, **122**, 15017–15025.

26 G. Nazira, M. F. Khana, I. Akhtarb, K. Akbara, P. Gautama, H. Noha, Y. Seo, S.-H. Chun and J. Eom, Enhanced photoresponse of ZnO quantum dot-decorated MoS_2 thin films, *RSC Adv.*, 2017, **7**, 16890–16900.

27 K. K. Paul, L. P. Mawlong and P. K. Giri, Trion-inhibited strong excitonic emission and broadband giant photoresponsivity from chemical vapor-deposited monolayer MoS_2 grown *in situ* on TiO_2 nanostructure, *ACS Appl. Mater. Interfaces*, 2018, **10**, 42812–42825.

28 J. Yan, C. Ma, P. Liu and G. Yang, Plasmon-induced energy transfer and photoluminescence manipulation in MoS_2 with a different number of layers, *ACS Photonics*, 2017, **4**, 1092–1100.

29 Y. Lin, E. Hathaway, F. Habis, Y. Wang, R. G. Rodriguez, K. Alnasser, N. Hurley and J. Cui, Enhanced Emission from Defect Levels in Multilayer MoS_2, *Adv. Opt. Mater.*, 2022, **10**, 2201059.

30 J.-W. Jiang and H. S. Park, Mechanical properties of MoS_2/graphene heterostructures, *Appl. Phys. Lett.*, 2014, **105**, 033108.

31 A. Ebnonnasir, B. Narayanan, S. Kodambaka and C. V. Ciobanu, Tunable MoS_2 bandgap in MoS_2-graphene heterostructures, *Appl. Phys. Lett.*, 2014, **105**, 031603.

32 D. Pierucci, H. Henck, J. Avila, A. Balan, C. H. Naylor, G. Patriarche, Y. J. Dappe, M. G. Silly, F. Sirotti, A. T. C. Johnson, M. C. Asensio and A. Ouerghi, Band Alignment and Minigaps in Monolayer MoS_2-Graphene van der Waals Heterostructures, *Nano Lett.*, 2016, **16**, 4054–4061.

33 C.-J. Shih, Q. H. Wang, Y. Son, Z. Jin, D. Blankschtein and M. S. Strano, Tuning On–Off Current Ratio and Field-Effect Mobility in a MoS_2–Graphene Heterostructure *via* Schottky Barrier Modulation, *ACS Nano*, 2014, **8**, 5790–5798.

34 J. Shi, M. Liu, J. Wen, X. Ren, X. Zhou, Q. Ji, D. Ma, Y. Zhang, C. Jin, H. Chen, S. Deng, N. Xu, Z. Liu and Y. Zhang, All Chemical Vapor Deposition Synthesis and Intrinsic

Bandgap Observation of MoS_2/Graphene Heterostructures, *Adv. Mater.*, 2015, **27**, 7086–7092.

35 M. G. Dastidar, N. Basu, I. H. Kao, J. Katoch, P. K. Nayak, S. Singh and V. P. Bhallamudi, Optically induced trion formation and its control in a MoS_2/graphene van der Waals heterostructure, *Nanoscale*, 2024, **16**, 19413–19421.

36 J. Jadczak, J. Kutrowska-Girzycka, M. Bieniek, T. Kazimierczuk, P. Kossacki, J. J. Schindler, J. Debus, K. Watanabe, T. Taniguchi and C. H. Ho, Probing negatively charged and neutral excitons in MoS_2/hBN and hBN/MoS_2/hBN van der Waals heterostructures, *Nanotechnology*, 2021, **32**, 145717.

37 T. Ahmed, K. Roy, S. Kakkar, A. Pradhan and A. Ghosh, Interplay of charge transfer and disorder in optoelectronic response in Graphene/hBN/MoS_2 van der Waals heterostructures, *2D Mater.*, 2020, **7**, 025043.

38 S. Wang, X. Wang and J. H. Warner, All Chemical Vapor Deposition Growth of MoS_2:h-BN Vertical van der Waals Heterostructures, *ACS Nano*, 2015, **9**, 5246–5254.

39 K. S. Novoselov, A. Mishchenko, A. Carvalho and A. H. Castro Neto, 2D materials and van der Waals heterostructures, *Science*, 2016, **353**, 461.

40 K. Nisi, J. C. Thomas, S. Levashov, E. Mitterreiter, T. Taniguchi, K. Watanabe, S. Aloni, T. R. Kuykendall, J. Eichhorn, A. W. Holleitner, A. Weber-Bargioni and C. Kastl, Scanning probe spectroscopy of sulfur vacancies and MoS_2 monolayers in side-contacted van der Waals heterostructures, *2D Mater.*, 2025, **12**, 05023.

41 S.-L. Chou, S.-Y. Lin, Y.-H. Wu, T.-P. Huang, M.-Y. Lin, Y.-Y. Lee, S.-C. Weng, H.-F. Chen and Y.-J. Wu, A Novel Method for Synthesis of Graphene Oxide Thin-film Utilizing Vacuum UV Exposure, *Opt. Mater.*, 2025, **160**, 116697.

42 S.-Y. Lin, S.-L. Chou, T.-P. Huang, M.-Y. Lin, H.-F. Chen, P. J. Sarre, C.-M. Tseng and Y.-J. Wu, Blue Luminescence from N-doped Graphene, *Astrophys. J.*, 2024, **977**, 230.

43 S.-L. Chou, W.-B. Shih, M.-Z. Yang, T.-P. Huang, S.-Y. Lin, M.-Y. Lin, W.-J. Huang, C. M. Chu, W.-Y. Woon, Y.-Y. Lee, Y.-P. Lee and Y.-J. Wu, A Plausible Model for the Galactic Extended Red Emission: Graphene Exposed to Far-Ultraviolet Light, *Astrophys. J.*, 2023, **944**, 18.

44 S.-L. Chou, M.-Y. Lin, T.-P. Huang, S.-Y. Lin, M.-Z. Yang, Y.-Y. Lee and Y.-J. Wu, Far-UV spectroscopy of mono-and multilayer hexagonal boron nitrides, *Spectrochim. Acta, Part A*, 2022, **270**, 120849.

45 S.-L. Chou, M.-Y. Lin, S.-Y. Lin, W.-J. Huang, T.-P. Huang, Y.-C. Lee and Y.-J. Wu, Far-ultraviolet absorption and photoluminescence of monolayer graphene and its implications for extended red emission, *Astrophys. J.*, 2020, **901**, 103.

46 B. C. Windom, W. G. Sawyer and D. W. Hahn, A Raman Spectroscopic Study of MoS_2 and MoO_3: Applications to Tribological Systems, *Tribol. Lett.*, 2011, **42**, 301–310.

47 H. Li, Q. Zhang, C. C. R. Yap, B. K. Tay, T. H. T. Edwin, A. Olivier and D. Baillargeat, From Bulk to Monolayer MoS_2: Evolution of Raman Scattering, *Adv. Funct. Mater.*, 2012, **22**, 1385–1390.

48 B. Chakraborty, A. Bera, D. V. S. Muthu, S. Bhowmick, U. V. Waghmare and A. K. Sood, Symmetry-dependent phonon renormalization in monolayer MoS_2 transistor, *Phys. Rev. B: Condens. Matter Mater. Phys.*, 2012, **85**, 161403(R).

49 J. Jadczak, J. Kutrowska-Girzycka, M. Bieniek, T. Kazimierczuk, P. Kossacki, J. J. Schindler, J. Debus, K. Watanabe, T. Taniguchi, C. H. Ho, A. Wójs, P. Hawrylak and L. Bryja, Probing negatively charged and neutral excitons in MoS_2/hBN and hBN/MoS_2/hBN van der Waals heterostructures, *Nanotechnology*, 2021, **32**, 145717.

50 T. Cheiwchanchamnangij and W. R. L. Lambrecht, Quasiparticle band structure calculation of monolayer, bilayer, and bulk MoS_2, *Phys. Rev. B: Condens. Matter Mater. Phys.*, 2012, **85**, 205302.

51 F. Wu, F. Qu and A. H. MacDonald, Exciton band structure of monolayer MoS_2, *Phys. Rev. B: Condens. Matter Mater. Phys.*, 2015, **91**, 075310.

52 C. Yim, M. O'Brien, N. McEvoy, S. Winters, I. Mirza, J. G. Lunney and G. S. Duesberg, Investigation of the optical properties of MoS_2 thin films using spectroscopic ellipsometry, *Appl. Phys. Lett.*, 2014, **104**, 103114.

53 K. M. Islam, R. Synowicki, T. Ismael, I. Oguntoye, N. Grinalds and M. D. Escarra, In-Plane and Out-of-Plane Optical Properties of Monolayer, Few-Layer, and Thin-Film MoS_2 from 190 to 1700 nm and Their Application in Photonic Device Design, *Adv. Photonics Res.*, 2021, **2**, 2000180.

54 S. Golovynskyi, I. Irfan, M. Bosi, L. Seravalli, O. I. Datsenko, I. Golovynska, B. Li, D. Lin and J. Qu, Exciton and trion in few-layer MoS_2: thickness- and temperature-dependent photoluminescence, *Appl. Surf. Sci.*, 2020, **515**, 146033.

55 T. Korn, S. Heydrich, M. Hirmer, J. Schmutzler and C. Schüller, Low-temperature photocarrier dynamics in monolayer MoS_2, *Appl. Phys. Lett.*, 2011, **99**, 102109.

56 H. Li, X. Zhu, Z. K. Tang and X. H. Zhang, Low-temperature photoluminescence emission of monolayer MoS on diverse substrates grown by CVD, *J. Lumin.*, 2018, **199**, 210–215.

57 X. Z. Du, J. Li, J. Y. Lin and H. X. Jiang, The origin of deep-level impurity transitions in hexagonal boron nitride, *Appl. Phys. Lett.*, 2015, **106**, 021110.

58 S. E. Panasci, I. Deretzis, E. Schilirò, A. La Magna, F. Roccaforte, A. Koos, M. Nemeth, B. Pécz, M. Cannas, S. Agnello and F. Giannazzo, Interface Properties of MoS_2 van der Waals Heterojunctions with GaN, *Nanomaterials*, 2024, **14**, 133.

59 S. E. Panasci, E. Schilirò, G. Greco, M. Cannas, F. M. Gelardi, S. Agnello, F. Roccaforte and F. Giannazzo, Strain, Doping, and Electronic Transport of Large Area Monolayer MoS_2 Exfoliated on Gold and Transferred to an Insulating Substrate, *ACS Appl. Mater. Interfaces*, 2021, **13**, 31248–31259.

60 A. Michail, N. Delikoukos, J. Parthenios, C. Galiotis and K. Papagelis, Optical detection of strain and doping inhomogeneities in single layer MoS_2, *Appl. Phys. Lett.*, 2016, **108**, 173102.

61 Y. Xu, L. Yan, J. Si, M. Li, Y. Ma, J. Li and X. Hou, Nonlinear absorption properties and carrier dynamics in MoS_2/

graphene van der Waals heterostructures, *Carbon*, 2020, **165**, 421–427.

62 Z. Xu, Z. Liu, D. Zhang, Z. Zhong and T. B. Norris, Ultrafast dynamics of charge transfer in CVD grown MoS_2–graphene heterostructure, *Appl. Phys. Lett.*, 2021, **119**, 093102.

63 J. Wang, H. Liu, X. Hu, Y. Liu and D. Liu, Imaging of Defect-Accelerated Energy Transfer in MoS_2/hBN/WS_2 Heterostructures, *ACS Appl. Mater. Interfaces*, 2022, **14**, 8521–8526.

64 H. Liu, T. Wang, C. Wang, D. Liu and J. Luo, Exciton Radiative Recombination Dynamics and Nonradiative Energy Transfer in Two-Dimensional Transition-Metal Dichalcogenides, *J. Phys. Chem. C*, 2019, **123**, 10087–10093.

65 H. Zehua, W. Zhangting, C. Han, J. He, Z. Ni and W. Chen, Two-Dimensional Transition Metal Dichalcogenides: Interface and Defect Engineering, *Chem. Soc. Rev.*, 2018, **47**, 3100–3128.